photonics

MDPI

Article

Study on the Influence of Mechanical Noise on the Impact Identification Performance of an FBG Accelerometer

Yong-Hao Liu [1], Zhi-Jian Jia [2], Chuan-Yu Guo [1], Jia Rui [2], Xiao-Wei Feng [3], Ji-Hong Wang [4,*], Hua-Ping Wang [1,*] and Ping Xiang [5,*]

[1] School of Civil Engineering and Mechanics, Lanzhou University, Lanzhou 730000, China; liuyh2020@lzu.edu.cn (Y.-H.L.); guochy2025@lzu.edu.cn (C.-Y.G.)
[2] Gansu Institute of Urban and Rural Planning and Design Institute Co., Ltd., Lanzhou 730070, China; gscxgh2016@163.com (Z.-J.J.); richard800910@163.com (J.R.)
[3] Gansu Provincial Transportation Science Research Institute Group Co., Ltd., Lanzhou 730030, China; 15309860930@163.com
[4] Gansu ZhiTong Technology Enginnering Detection Consulting Co., Ltd., Gansu Province Highway Engineering Intelligent Inspection and Testing Technology Innovation Center, Lanzhou 730050, China
[5] School of Civil Engineering, Central South University, Changsha 410075, China
* Correspondence: gszt1998@126.com (J.-H.W.); wanghuaping1128@sina.cn or hpwang@lzu.edu.cn (H.-P.W.); pxiang2-c@my.cityu.edu.hk (P.X.)

Abstract

The influence of mechanical noise on impact identification using fiber Bragg grating (FBG) accelerometers in complex environments remains insufficiently explored and quantitatively characterized. This study investigates how the intensity and propagation path of mechanical noise affect the output stability and impact-detection capability of a self-developed FBG accelerometer. A quantitative evaluation approach is established using wavelength-variation statistics, impact-response amplitude, and signal-to-noise ratio (SNR). Experimental results show that mechanical noise markedly increased the background wavelength fluctuation, with the maximum standard deviation reaching 16.71 pm, approximately 11 times the no-additional-noise value. By contrast, the RMS of the target impact response increased only slightly, from 0.0300 nm to 0.0353 nm, indicating that mechanical noise primarily affects baseline stability rather than the amplitude of the target impact response. Under the highest-intensity disturbance tested, the SNR remained at 22.98 dB, and the impact event remained distinguishable. The proposed multi-indicator approach provides a quantitative characterization of the FBG accelerometer response under different mechanical-noise conditions. A commercial 941B accelerometer was used as an external reference for sensitivity calibration, and its measurements were not used for direct performance comparison with the FBG accelerometer. The results provide experimental evidence of the impact-identification behavior of the proposed sensor under the investigated mechanical-noise conditions.

Keywords: FBG accelerometer; mechanical noise environment; impact identification; background fluctuation; signal-to-noise ratio

Check for updates

Received: 6 August 2026
Revised: 4 September 2026
Accepted: 16 September 2026
Published: 21 September 2026

Copyright: © 2026 by the authors. Licensee MDPI, Basel, Switzerland. This article is an open access article distributed under the terms and conditions of the Creative Commons Attribution (CC BY) license.

1. Introduction

With the increasing demand for reliability and intelligent operation in large-scale engineering structures, aerospace systems, and complex mechanical equipment, real-time monitoring of structural states and dynamic responses has become essential for ensuring safe operation. During long-term service, structures are inevitably exposed to vibration,

impact, and environmental disturbances, which can lead to accumulated fatigue damage and even cause localized failure. Therefore, reliable and stable measurement of dynamic responses is of great importance for structural health monitoring (SHM). Conventional electrical accelerometers may face limitations in environments with high intensity electromagnetic interference, harsh operation conditions, or long transmission distances. In contrast, fiber Bragg grating (FBG) sensors offer several advantages, including immunity to electromagnetic interference, low weight, corrosion resistance, multiplexing capability, and suitability for harsh environments, and have therefore attracted considerable attention in optical fiber sensing [1–6]. FBG sensors measure stress, temperature, and dynamic loads through changes in the grating period and effective refractive index induced by external perturbations, and they have been widely applied to the health monitoring of aerospace composites and civil engineering structures [7–11]. FBG accelerometers convert mechanical acceleration into optical wavelength shifts through an inertial mass and an elastic sensing structure, providing promising capabilities for vibration and impact monitoring. Because the FBG serves as a strain-sensitive element, its dynamic performance depends strongly on the sensor packaging configuration and strain-transfer path. Achieving an appropriate balance among sensitivity, frequency response, and structural stability is therefore a key challenge in FBG accelerometer design.

In recent years, extensive research has focused on cantilever beams, flexure hinges, multi-beam configurations, and multi-axis sensing structures. Improvements in sensing performance have been achieved by optimizing the stiffness of elastic elements, the parameters of inertial masses, and the strain-transfer paths [12–20]. In practical engineering applications, however, FBG dynamic signals are often contaminated by equipment operation, structural vibration, and environmental disturbances, which can obscure the characteristics of target impact events. Consequently, improving sensor sensitivity alone is insufficient for complex operating conditions. It is also necessary to understand how FBG accelerometers respond to mechanical noise and to establish quantitative methods for evaluating their resistance to interference.

FBG accelerometers generally employ an “inertial mass–elastic sensing element–FBG strain conversion” configuration. External acceleration generates an inertial force that deforms the elastic sensing structure and produces a shift in the FBG center wavelength. Because the sensor output is directly affected by structural parameters, structural optimization remains a major strategy for improving FBG accelerometer performance. Guo et al. systematically reviewed the development of FBG accelerometers and noted that sensitivity, natural frequency, and dynamic range are governed mainly by the matching relationship among the inertial mass, elastic structure, and packaging configuration [12]. Hong et al. proposed a low-frequency FBG accelerometer based on multiple cantilever beams, improving low-frequency vibration detection through structural optimization and providing a new design for complex vibration environments [13]. Flexible sensing structures have subsequently become an important research direction. Reghuprasad et al. used serially connected cantilever beams to optimize an FBG accelerometer and experimentally investigated the effects of structural parameters on its dynamic response [14]. Wang et al. studied a miniaturized FBG accelerometer for low-frequency vibration monitoring and demonstrated stable measurements [15]. Lightweight structures, flexure-hinge configurations, and biaxial sensing structures have also been developed to improve sensitivity and directional dis-crimination [16–20]. Although these studies have substantially advanced FBG accelerometer design, most have focused on the sensor structure itself, with comparatively limited attention to the influence of mechanical noise on signal quality in practical applications. A systematic investigation of sensor responses under complex mechanical disturbances is therefore still needed.

Impact loads are typically characterized by short durations, broad frequency content, and pronounced transient features, and they can initiate and propagate structural damage. Rapid and reliable impact detection is therefore important for the safety assessment of aerospace composites and engineering structures. Owing to their high sensitivity and good compatibility with host structures, FBG sensors have been widely used for impact monitoring of composite materials. Li et al. combined embedded FBG sensors with ensemble learning to identify impact states in CFRP structures, thereby improving impact detection for complex structures [21]. Huan et al. investigated low-velocity impact monitoring of composite tubes using FBG sensors and confirmed their ability to capture transient responses [22]. With advances in signal processing, FBG-based impact monitoring has evolved from simple event detection toward impact localization and load identification. Ding et al. proposed an FBG-based impact localization method combining wavelet-threshold denoising with an outlier-identification algorithm for low-velocity impacts on CFRP laminates [23]. Huang et al. combined a single FBG sensor with variational mode decomposition (VMD) to achieve robust identification of impact forces on composite structures, reducing sensing-system complexity [24]. However, most existing studies have been conducted under controlled laboratory conditions, with limited consideration of mechanical noise in real operating environments. As background vibration increases, impact-related features in the FBG output may be partially masked, thereby reducing detection reliability.

Dynamic monitoring in complex mechanical environments is commonly affected by random vibration, equipment operating noise, and other environmental disturbances. For FBG sensing systems, such interference can reduce the signal-to-noise ratio (SNR) and may also compromise impact-feature extraction and event identification. Accordingly, noise suppression and signal enhancement have received increasing attention. Liu et al. proposed an improved spectral-subtraction method for handling additive noise in FBG-based condition-monitoring systems, effectively reducing the influence of noise on the measured signals [25]. Time-frequency analysis and adaptive decomposition methods have also been widely used for complex vibration signals; among them, variational mode decomposition (VMD) is effective for non-stationary signals and can enhance feature extraction [26]. In structural health monitoring, signal-processing techniques have consequently become important tools for improving detection reliability. Previous studies have shown that combining time-frequency analysis, feature enhancement, and intelligent recognition algorithms can improve the interpretation of dynamic signals under high-intensity noise conditions [27–29]. Nevertheless, existing work has focused mainly on noise-removal algorithms, while systematic investigations of FBG response evolution under different noise intensities, SNR degradation, and quantitative anti-noise performance remain limited.

In summary, substantial progress has been made in FBG accelerometer structural design, impact monitoring, and signal-processing techniques. However, several gaps remain in the application of FBG-based impact monitoring under complex mechanical noise conditions:

- First, existing studies on FBG accelerometers have focused primarily on sensitivity, frequency response, and structural optimization, whereas the relationship between sensor design characteristics and adaptability to mechanical noise has received insufficient attention.
- Second, most FBG impact-monitoring studies have been conducted under controlled laboratory conditions, and the evolution of impact signals and the associated degradation in detection performance under mechanical background noise have not been examined in sufficient depth.

- Third, a quantitative evaluation framework for the anti-noise capability of FBG impact monitoring is still lacking, making it difficult to characterize sensing-performance changes under different noise conditions in a systematic manner.

To address these gaps, this study investigates a proposed FBG accelerometer for impact monitoring under controlled mechanical-noise conditions. By introducing noise with different excitation intensities and propagation paths, the effects of mechanical disturbance on the time-domain and frequency-domain characteristics of the FBG dynamic response and on the SNR are examined. A multi-indicator evaluation approach is then established to characterize the anti-interference performance of the sensor, providing an experimental basis for applying FBG accelerometers to impact and structural-dynamic monitoring in complex environments.

2. FBG Accelerometer Structural Design and Experimental System

2.1. Structure and Working Principle of the FBG Accelerometer

An FBG accelerometer independently developed by our research group was used as the sensing device in this study. The sensor consisted of a flexible elastic body containing an integrated fiber Bragg grating and an inertial mass block. When subjected to external impact or vibration, the mass block undergoes relative displacement under the resulting inertial force, producing a small deformation of the elastic body. This deformation changes the axial strain of the FBG and consequently shifts its Bragg center wavelength. A high-speed FBG interrogator records the wavelength variation in real time, and the corresponding acceleration is obtained using the calibrated sensor sensitivity, enabling dynamic impact measurements. The sensor adopts a compact, lightweight, and integrated single-material structure consisting of a cylindrical elastic body, an inertial mass region, and an axially embedded FBG. The elastic body had a radius of 5 mm and a height of 25 mm, while the inertial mass region had a radius of 15 mm and a height of 15 mm. The total mass of the sensor was 12.6 g. The integrated structure was fabricated entirely from cured 184 silicone elastomer, providing a continuous mechanical load-transfer path between the inertial mass and the embedded FBG. The FBG is embedded along the central axis of the elastic body to facilitate axial strain transfer.

For mechanical analysis, the sensor was modeled as a flexible distributed elastic body carrying a concentrated inertial mass. As shown in Figure 1b–d, the axial displacement of the elastic body is denoted by $u(z,t)$, while $N(z,t)$ represents the axial internal force. A differential element of the elastic body is considered to establish the force-equilibrium relationship, and the inertial mass is represented by a concentrated mass with displacement $U(L,t)$. This model describes the dynamic force-transfer process from the inertial mass through the elastic body to the embedded FBG and provides the mechanical basis for relating external acceleration to the measured wavelength response. Compared with previously reported FBG accelerometers based mainly on cantilever beams, diaphragms, or flexure-hinge structures [12–20], the present sensor uses a cylindrical elastic sensing body with an axially embedded FBG and an integrated inertial mass region. The resulting structure has a compact geometry and a total mass of 12.6 g. The use of a single silicone elastomer material also simplifies the mechanical configuration and provides a continuous load-transfer path from the inertial mass to the FBG. These structural characteristics provide a suitable platform for investigating the response of an FBG accelerometer under different mechanical-noise conditions. In this study, particular attention is given to the effects of excitation intensity and propagation path on impact identification.

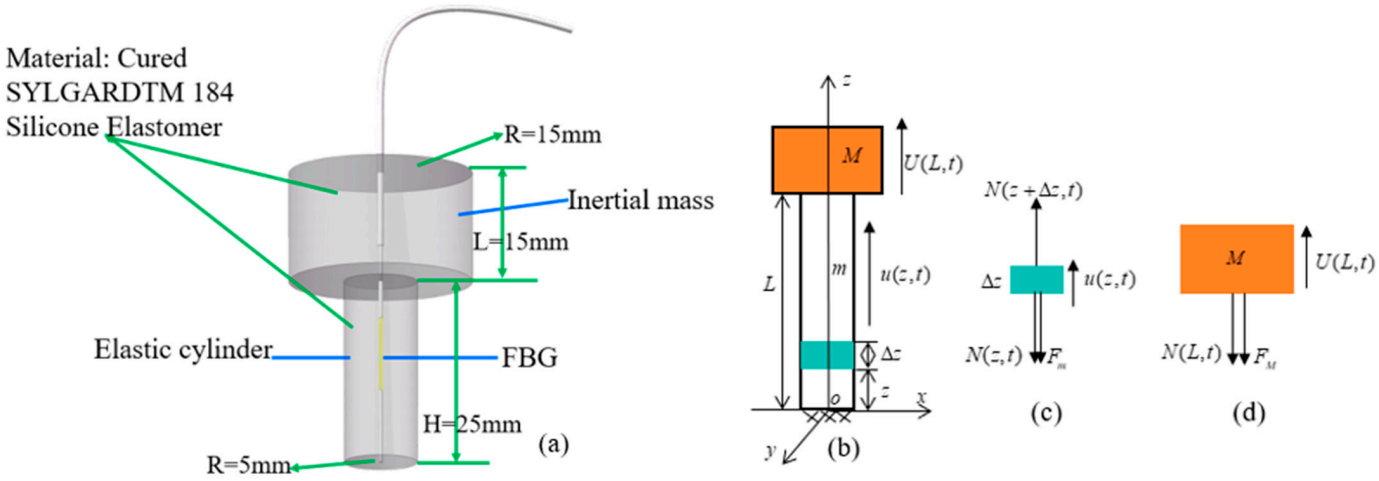


Figure 1. Structural configuration and mechanical model of the FBG accelerometer: (**a**) physical structure and key dimensions; (**b**) overall mechanical model; (**c**) differential element of the elastic body; and (**d**) inertial mass equilibrium.

The acceleration sensitivity of the FBG accelerometer was calibrated using a commercial Hengxin Hongce 941B accelerometer as the reference instrument. The two accelerometers were installed at structurally symmetric positions on the specimen and subjected to the same periodic impact excitation. Considering the symmetric arrangement and identical excitation conditions, the acceleration amplitudes at the two measurement locations were assumed to be equivalent. The peak acceleration measured by the 941B accelerometer was taken as the reference acceleration, while the corresponding peak wavelength variation measured by the FBG accelerometer was used as the optical response. The sensitivity was calculated as the ratio of the wavelength variation to the reference acceleration, yielding a calibrated sensitivity of 939.3 pm/g. The calibration employed the same periodic impact loading used in the present study, with an impact repetition frequency of 0.375 Hz, rather than a frequency-swept excitation. This calibrated sensitivity was subsequently used to convert the measured wavelength variations into acceleration responses, as described in Section 4.5.3.

2.2. Experimental System

To investigate the influence of mechanical noise on the impact identification performance of the FBG accelerometer, an experimental system was established, as shown in Figures 2 and 3. The system comprised the FBG accelerometer, a CFRP plate specimen, fixing fixtures, a high-speed FBG interrogator, and a computer-based data acquisition system.

During the experiments, both ends of the CFRP plate were rigidly clamped to pro-vide stable boundary conditions. The FBG accelerometer was mounted at a designated measurement location on the specimen and connected to the high-speed FBG interrogator through an optical fiber. The interrogator recorded the FBG center-wavelength variations in real time and transmitted the data to a host computer for display, storage, and subsequent analysis.

The target impact was applied periodically at a frequency of 0.375 Hz to ensure consistent excitation across all test cases. Mechanical background noise was introduced by striking either a metal pipe or the test-bench tabletop with low or high-intensity mechanical excitation near the experimental platform. Striking the pipe was intended to simulate vibration transmission through industrial piping and equipment, whereas striking the test bench was intended to simulate structural vibration transmitted through the experimental platform. For all noise conditions, the target impact was kept unchanged, while only

the noise source and excitation intensity were varied, thereby implementing a controlled-variable experimental design.

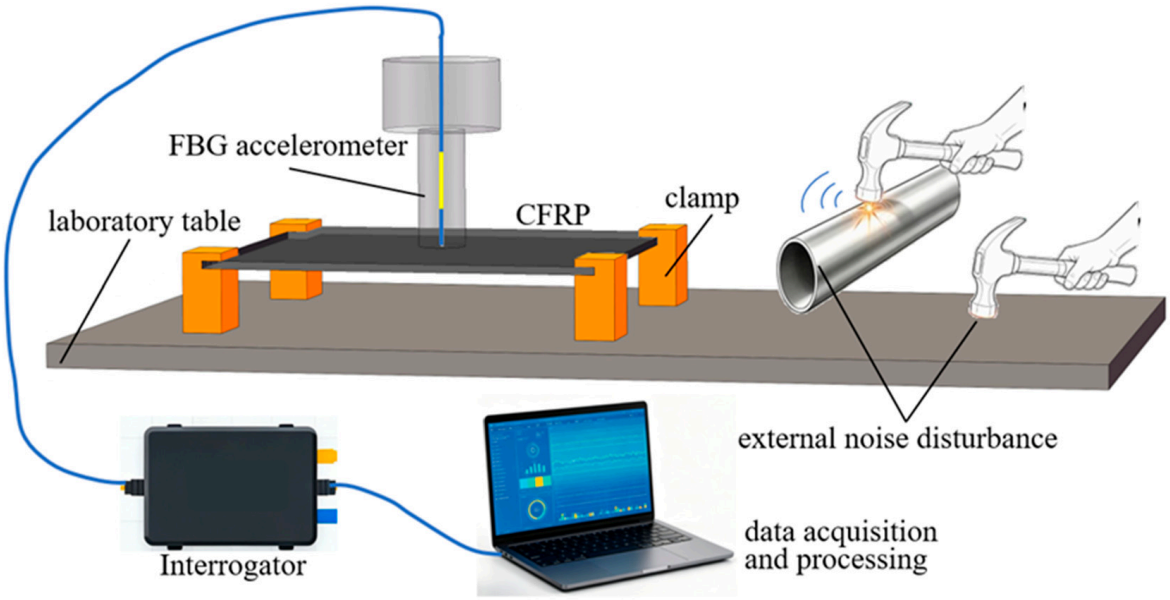


Figure 2. Schematic diagram of the experimental system.

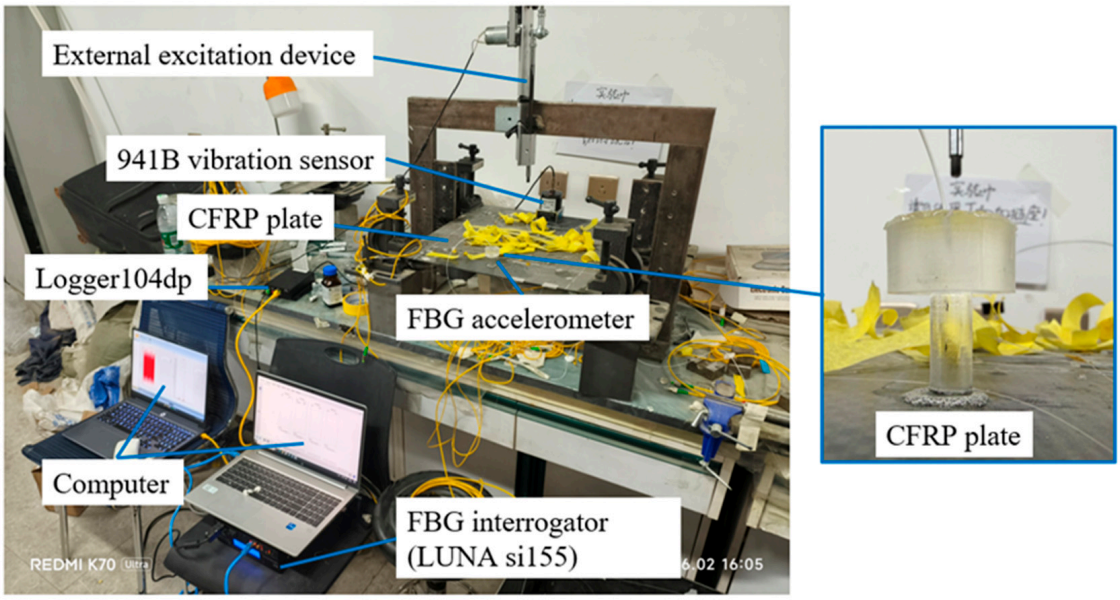


Figure 3. Photograph of the experimental system.

The same sampling parameters and sensor mounting configuration were used for all test cases to ensure experimental comparability. The measured acceleration responses were then analyzed to characterize the impact response and the resistance of the FBG accelerometer to different levels and propagation paths of mechanical interference.

Five experimental test cases were designed to systematically investigate the effect of mechanical noise on impact identification. The sensor mounting position, sampling parameters, and target impact conditions were kept constant in all cases, while the noise source and excitation intensity were varied. The experimental scheme is summarized in Table 1.

Table 1. Experimental test-case design.

Test Case	Target Impact	Mechanical Excitation	Propagation Path	Repetitions	Duration
Case1	Applied	None	—	4	60 s
Case2	Applied	Low-intensity excitation	Pipe	4	60 s
Case3	Applied	Low-intensity excitation	Test bench	4	60 s
Case4	Applied	High-intensity excitation	Pipe	4	60 s
Case5	Applied	High-intensity excitation	Test bench	4	60 s

Four independent experimental runs were conducted for each test case as shown in Figure 4. Each run lasted 60 s. During each run, the target impact was applied periodically at an impact repetition frequency of 0.375 Hz, while the corresponding mechanical-noise condition was maintained throughout the acquisition period. The same sensor mounting configuration and sampling parameters were used in all repeated runs. Representative results from one experimental run for each test case are presented in the subsequent figures and tables for clarity.

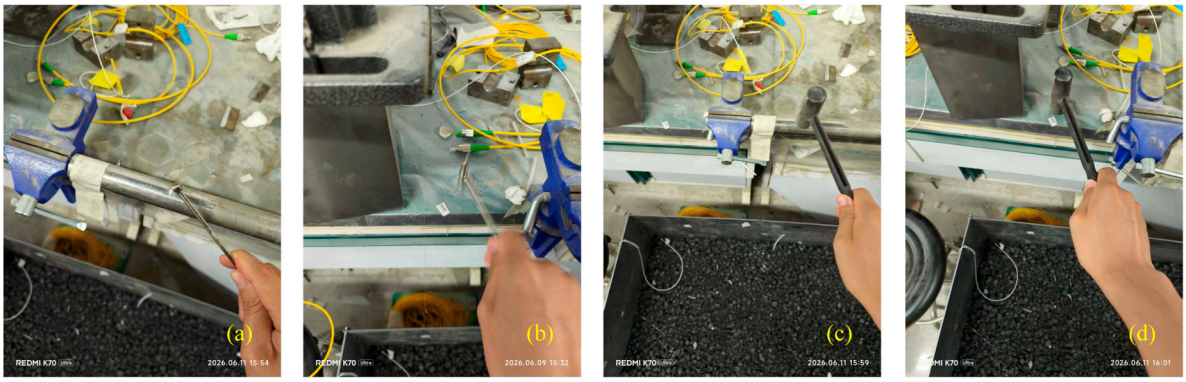


Figure 4. Experimental configurations for the four mechanical-noise conditions: (**a**) low-intensity pipe excitation; (**b**) low-intensity test-bench excitation; (**c**) high-intensity pipe excitation; and (**d**) high-intensity test-bench excitation.

3. Analysis of Impact Response Characteristics of the FBG Accelerometer Under No Additional Noise Conditions

To characterize the baseline impact response of the FBG accelerometer and provide a reference for the subsequent noise experiments, periodic impact tests were first conducted without additional external mechanical noise. The target impact was applied at 0.375 Hz, and the FBG wavelength variation was recorded in real time using the optical fiber interrogator. The wavelength response was converted into acceleration using the calibrated sensor sensitivity. The corresponding results are shown in Figure 5.

As shown in Figure 5, the FBG accelerometer responded clearly to each impact under the no-additional-noise condition. Distinct acceleration peaks with similar amplitudes were observed, indicating good repeatability. Following each impact, the response returned rapidly toward the baseline, with limited baseline fluctuation and no obvious drift or abnormal disturbance. These features indicate that the experimental system provided a stable, low-noise measurement environment. A magnified view of the first impact response is presented in Figure 5b, from which three characteristic stages can be identified: the impact-loading stage, the high-frequency transient-vibration stage, and the damped free-decay stage.

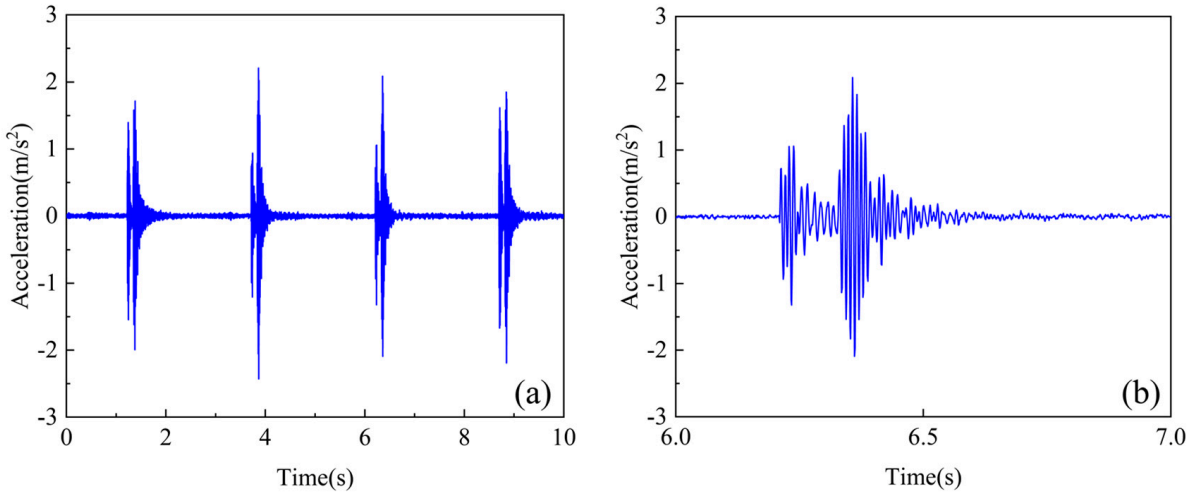


Figure 5. (**a**) Overall and (**b**) enlarged acceleration responses without external mechanical noise.

(1) Impact-loading stage: When the impact is applied, the structure is excited almost instantaneously. The inertial mass responds rapidly to the induced inertial force, producing a transient deformation of the elastic body. The FBG center wavelength shifts accordingly, and a sharp transient peak appears in the acceleration response. Because the impact duration is very short, both the rising and falling edges of the response exhibit large rates of change, demonstrating the sensor's ability to capture transient impact events.

(2) High-frequency transient-vibration stage: After the impact ends, the structure and sensor continue to vibrate because of inertia, producing several oscillation cycles. As shown in Figure 5, pronounced periodic oscillations remain after the impact peak, but their amplitude decays rapidly as the impact energy is dissipated by the elastic body, inertial mass, and host structure. The flexible elastic sensing element also provides viscoelastic damping, which helps suppress sustained oscillations and limits the persistence of resonance that could interfere with subsequent impact identification.

(3) Damped free-decay stage: As the system continues to dissipate energy, the acceleration amplitude gradually decreases and approaches zero. The decay process is smooth, without secondary impacts or abnormal oscillations, indicating stable dynamic behavior. The rapid recovery of the response is beneficial for identifying successive impact events because it reduces interference from residual vibration generated by preceding impacts.

The impact response exhibits alternating positive and negative oscillations, which is consistent with the behavior of an underdamped mass–elastic system. Following the impact, the inertial mass and elastic body undergo free vibration under the combined effects of inertial and restoring forces. As damping dissipates the vibration energy, the oscillation amplitude gradually decreases and eventually stabilizes. This response is consistent with the dynamic characteristics expected from the sensor configuration and provides experimental support for the adopted structural design.

Overall, the no-additional-noise tests showed stable sensor output, distinct impact peaks, complete response waveforms, and good repeatability across successive impacts. These results provide a baseline for evaluating the effect of mechanical noise on impact identification in the following sections.

4. Influence of Mechanical Noise on Impact Identification Performance

Building on the no-additional-noise tests in Section 3, four mechanical-noise conditions were introduced to evaluate the impact identification performance of the FBG accelerometer under different disturbance levels and propagation paths. A low or high-intensity mechanical excitation was used to excite either a metal pipe or the test-bench tabletop, producing

four combinations of excitation intensity and transmission path. The resulting acceleration responses were compared in the time domain before the quantitative anti-noise assessment.

4.1. Case 2: Low-Intensity Pipe-Transmitted Mechanical Noise

Figure 6 presents the representative time-domain response under low-intensity mechanical excitation transmitted through the metal pipe. In this condition, the pipe was repeatedly excited near the experimental platform, generating background mechanical vibration that propagated toward the sensor location. The target impact conditions were kept unchanged from those in Section 3.

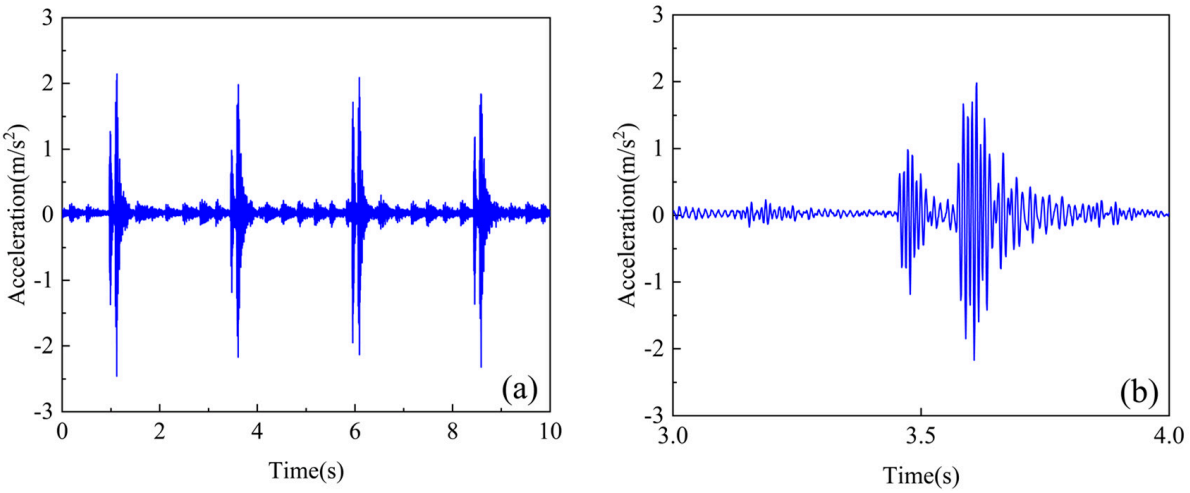


Figure 6. (**a**) Overall and (**b**) enlarged acceleration responses under Case 2 (low-intensity mechanical excitation of the pipe).

Under low-intensity mechanical excitation of the pipe, the background acceleration fluctuation increased relative to the no-additional-noise condition. The pipe provides a continuous structural path along which vibration can propagate, producing a more pronounced response at the sensor mounting location. In addition, coupling between the pipe's structural modes and the excitation may concentrate part of the mechanical energy and increase the disturbance transmitted to the sensing structure.

The background wavelength fluctuation was higher than that under the no-additional-noise condition, whereas the target impact peak changed only slightly. These observations indicate that low intensity pipe-propagated vibration mainly affects base-line stability while having a limited effect on the amplitude of the target impact response. The comparison also suggests that the propagation path of mechanical noise is an important factor in sensor disturbance, in addition to excitation intensity. Overall, the low intensity pipe-induced disturbance had only a limited influence on impact identification.

4.2. Case 3: Low-Intensity Test-Bench-Transmitted Mechanical Noise

Figure 7 shows the acceleration response when a low-intensity mechanical excitation was used to excite the test bench. Compared with the pipe-excitation condition, the mechanical transmission path through the test bench is shorter. The vibration was first introduced into the experimental platform and then transmitted to the specimen through the supporting structure, resulting in different background-noise characteristics. Although the background vibration increased, the target impact peak remains clearly distinguishable, the impact timing remains stable, and the subsequent free-decay response remains complete.

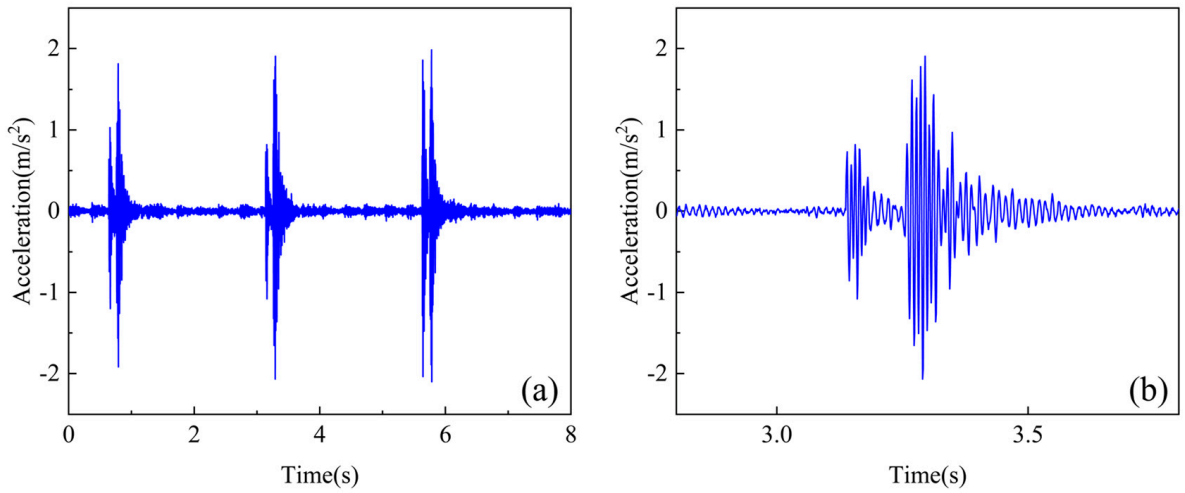


Figure 7. (**a**) Overall and (**b**) enlarged acceleration responses under Case 3 (low-intensity mechanical excitation of the test bench).

The test bench was a relatively rigid structure with high local stiffness, so a substantial portion of the impact energy was dissipated during propagation and only part of it reached the sensor location. Consequently, the background disturbance was relatively short-lived and had little influence on target impact identification. Under this low-intensity test-bench disturbance, the FBG accelerometer therefore retained a clear and stable impact response.

4.3. Case 4: High-Intensity Pipe-Transmitted Mechanical Noise

To further evaluate the sensor under high intensity mechanical disturbance, a high-intensity mechanical excitation was used to excite the metal pipe. The corresponding response is shown in Figure 8.

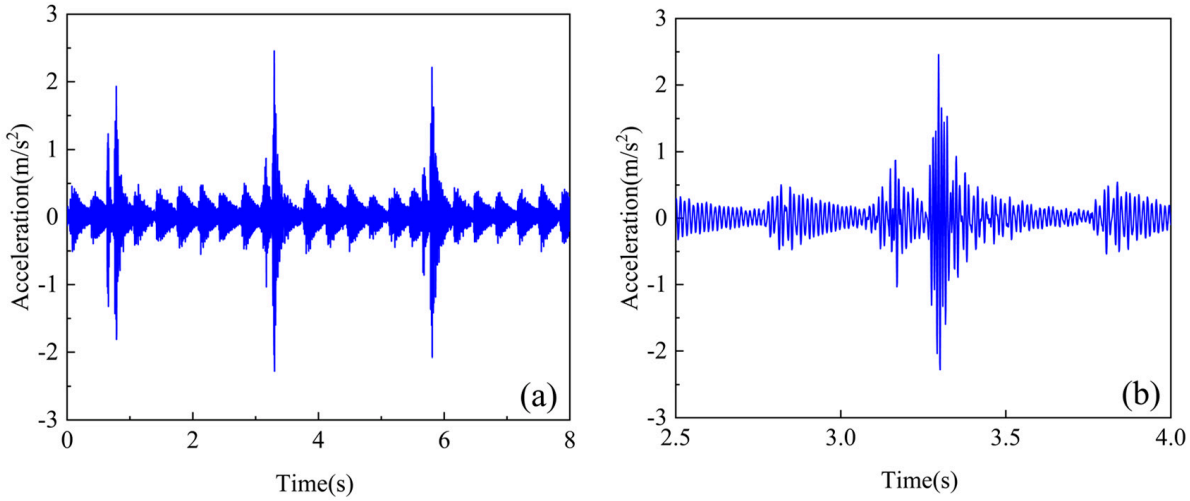


Figure 8. (**a**) Overall and (**b**) enlarged acceleration responses under Case 4 (high-intensity mechanical excitation of the pipe).

High-intensity mechanical excitation of the pipe produced the highest mechanical-noise condition in the experiment. Under this condition, the background wavelength variation was largest and the output fluctuation was most pronounced. Three factors con-tributed to this behavior:

- The high-intensity mechanical excitation input introduced greater mechanical energy and therefore produced a larger structural vibration amplitude;

- The pipe provides an effective structural path for vibration transmission, allowing mechanical energy to propagate toward the sensor location;
- The experimental results indicate that the pipe-transmitted excitation produced a higher disturbance at the sensor location under the tested conditions.

This condition represents a relatively severe mechanical-noise environment involving high-intensity equipment or pipeline vibration and external mechanical excitation. Despite the increased background disturbance, the target impact response remained characterized by a distinct transient peak, indicating that the FBG accelerometer can still identify the target event under high intensity pipe-propagated vibration.

4.4. Case 5: High-Intensity Test-Bench-Transmitted Mechanical Noise

Under high-intensity mechanical excitation of the test bench as shown in Figure 9, the vibration amplitude of the experimental platform increased because of the greater mechanical input. Compared with the corresponding low-intensity mechanical excitation condition, the background wavelength variation range increased further, indicating higher disturbance to the sensor output. Nevertheless, the target impact peak remained relatively stable. The key distinction is that the background disturbance and the target event differ in temporal characteristics: mechanical noise tends to appear as sustained or periodic vibration, whereas an impact produces a transient, high-amplitude response. This difference allows the target impact to remain identifiable even as the background noise increases.

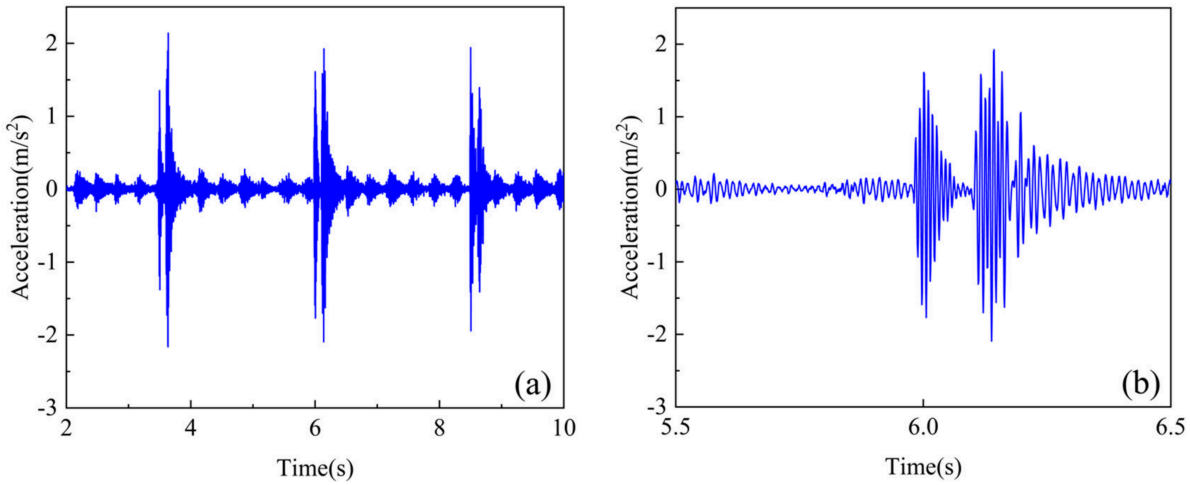


Figure 9. (**a**) Overall and (**b**) enlarged acceleration responses under Case 5 (high-intensity mechanical excitation of the test bench).

4.5. Quantitative Evaluation of Anti-Mechanical-Noise Performance of the FBG Accelerometer

4.5.1. Stability Analysis of Wavelength Variation

To ensure a consistent basis for comparison, background noise was evaluated using the wavelength-variation data recorded during the 1.0 s interval immediately preceding each target impact. The mean wavelength variation (mean), standard deviation (STD), and root-mean-square value of the background noise (noise RMS) were calculated, and the results are summarized in Table 2.

Mean of wavelength variation:

$$\overline{\Delta\lambda} = \frac{1}{N}\sum_{i=1}^{N}\Delta\lambda_i \quad (1)$$

Standard deviation of wavelength variation:

$$\sigma_{\Delta\lambda} = \sqrt{\frac{1}{N-1}\sum_{i=1}^{N}\left(\Delta\lambda_i - \overline{\Delta\lambda}\right)^2} \tag{2}$$

RMS of background noise:

$$RMS = \sqrt{\frac{1}{N}\sum_{i=1}^{N}\Delta\lambda_i^2} \tag{3}$$

Representative results from one experimental run for each test case are presented in Tables 2–5. Four independent experimental runs were conducted for each case, as described in Section 2.2. The reported values are from a representative single-run measurement.

As shown in Table 2, the no-additional-noise condition yielded a mean background wavelength variation close to zero, an STD of 1.46 pm, and a noise RMS of 1.49 pm, indicating low baseline fluctuation and good static stability of the measurement system.

As the external mechanical disturbance became stronger, the STD generally increased. The lowest STD occurred under the no-additional-noise condition, whereas the high-intensity mechanical excitation of the pipe condition produced the maximum STD of 16.71 pm, approximately 11 times the noise-free value. This result confirms that mechanical noise substantially increased background fluctuations in the FBG output. Under the same excitation intensity, the pipe-excitation condition consistently produced a larger STD than the test-bench condition, highlighting the influence of the transmission path. Compared with the test bench, the pipe provides a more continuous structural path with less vibration attenuation, leading to stronger mechanical coupling at the sensor location.

Table 2. Wavelength-variation stability under different test cases.

Test Case	Mean (pm)	STD (pm)	Noise RMS (pm)
Case1	−0.03	1.46	1.49
Case2	2.63	5.49	6.09
Case3	−0.03	2.28	2.31
Case4	0.06	16.71	16.71
Case5	0.03	6.72	6.73

Table 3. Impact wavelength response analysis under different test cases.

Test Case	Peak (nm)	Pmax-Pmin (nm)	RMS (nm)
Case1	0.2005	0.4001	0.03
Case2	0.2076	0.3973	0.0316
Case3	0.1983	0.3809	0.0302
Case4	0.2354	0.4536	0.0338
Case5	0.2005	0.3851	0.0353

Table 4. Acceleration response analysis under different test cases.

Test Case	Peak (m/s^2)	Pmax-Pmin (m/s^2)	RMS (m/s^2)
Case1	2.09	4.18	0.31
Case2	2.17	4.15	0.33
Case3	2.07	3.98	0.32
Case4	2.46	4.73	0.35
Case5	2.09	4.02	0.37

Table 5. Signal-to-noise ratio under different test cases.

Test Case	Signal-to-Noise Ratio (SNR) (dB)
Case1	42.58
Case2	30.65
Case3	38.67
Case4	22.98
Case5	29.48

4.5.2. Impact Response Analysis

For the impact-response analysis, the data window extended from 0.2 s before the impact to 0.3 s after the response had decayed to near zero.

As shown in Table 3, the impact peak remained relatively stable across the five test cases, with values close to 0.20 nm. This indicates that the external mechanical noise had no substantial effect on the amplitude of the target impact response.

The peak-to-peak response (Pmax-Pmin) ranged from 0.3809 to 0.4536 nm, with the largest value occurring under the high intensity pipe-excitation condition. This slight increase suggests that high-intensity noise can perturb the post-impact free-decay response, although the overall waveform remains intact. The impact-response RMS ranged from 0.0300 to 0.0353 nm and changed only slightly among the test cases. These results indicate that external mechanical noise affects background stability more strongly than the amplitude of the target impact response. The transient nature and relatively high energy of the impact event allow it to remain distinguishable from the background vibration in the time domain.

4.5.3. Acceleration Response Analysis

For the FBG accelerometer, the acceleration can be calculated from the wavelength response using the sensitivity relationship $S = \frac{\Delta\lambda_B}{a}$, and, by substituting the calibrated sensitivity of 939.3 pm/g into the values in Table 3, the peak acceleration during each impact can be obtained.

The calculated acceleration responses exhibited the same overall variation pattern as the corresponding wavelength responses. Accordingly, the peak acceleration, peak-to-peak acceleration, and RMS acceleration showed trends consistent with those of the wavelength response. The results indicate that external mechanical noise had little effect on the peak impact acceleration, although it caused a modest increase in background acceleration fluctuations.

4.5.4. Signal-to-Noise Ratio (SNR) Analysis

SNR calculation:

$$SNR = 20\log_{10}\left(\frac{Peak}{RMS_{noise}}\right) \quad (4)$$

where $Peak$ is the peak impact response, and RMS_{noise} is the background RMS value in the 1 s period before the impact.

As shown in Table 5 and Figure 10, the SNR was 42.58 dB under the no-additional-mechanical-noise condition. The SNR decreased as the background mechanical disturbance increased. The lowest value, 22.98 dB, was obtained under the high-intensity pipe-excitation condition, where the background fluctuation was also the largest. The target impact remained distinguishable under this condition.

In this study, 20 dB is used only as a practical reference level for discussing signal discernibility. It is not treated as a universal detection threshold for FBG-based impact monitoring. The required SNR may depend on the sensing configuration, signal-processing

procedure, target-event characteristics, and application conditions. Since SNR levels below 20 dB were not systematically investigated, the impact-identification performance under lower-SNR conditions cannot be determined from the present experiments.

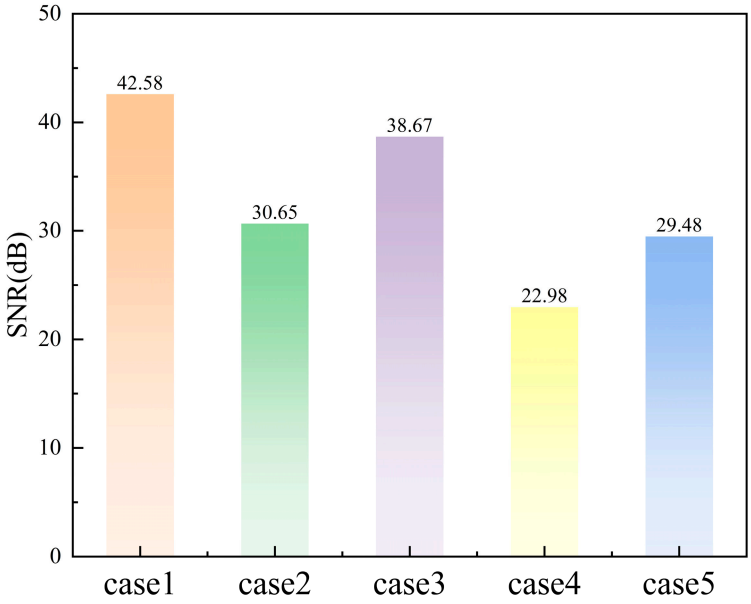


Figure 10. SNR bar chart under different test cases.

4.6. Discussion

The experimental results reveal that mechanical noise affects the background stability of the FBG accelerometer more strongly than the main amplitude of the target impact response. As the excitation intensity increased, the background wavelength fluctuation increased markedly, with the STD increasing from 1.46 pm under the no-additional-noise condition to 16.71 pm under high-intensity pipe excitation. In comparison, the RMS of the target impact response remained within 0.0300–0.0353 nm. This difference suggests that the transient impact response was relatively stable under the tested disturbance conditions, whereas the background response was more sensitive to externally introduced mechanical vibration. The reduction in SNR with increasing disturbance can therefore be associated mainly with the growth of the background component. The lowest SNR of 22.98 dB was obtained under high-intensity pipe excitation, where the background fluctuation was also the largest.

The observed response is consistent with the characteristics of the FBG sensing structure. The proposed accelerometer uses an inertial mass and a compliant elastic body to transfer external acceleration to the embedded FBG. Previous studies have shown that the dynamic behavior of FBG accelerometers is strongly affected by the mechanical configuration, inertial mass, elastic stiffness, and strain-transfer path [12–20]. These studies have mainly focused on improving sensitivity, frequency response, miniaturization, and directional response. FBG sensors have also been widely used for impact monitoring, impact localization, and impact-force identification in composite structures [21–24]. Recent studies have further demonstrated the use of FBG sensing for monitoring the mechanical and fatigue-related behavior of CFRP structures [30]. The present results extend these studies from sensor design and impact response toward the influence of mechanically generated background disturbances. In particular, the comparison between the pipe and test-bench excitation conditions shows that the propagation path can significantly affect the disturbance received by the sensor. FBG-based impact monitoring has also been demonstrated for CFRP laminates using embedded and surface-bonded sensing configurations [31]. In

the present study, the comparison between the pipe and test-bench excitation conditions shows that the propagation path can significantly affect the disturbance received by the sensor. Under both excitation levels, the pipe condition produced a larger background fluctuation than the corresponding test-bench condition. This indicates that the mechanical connection between a disturbance source and the sensing location should be considered when evaluating FBG accelerometers in practical environments.

The results also have implications for impact identification. The target impact remained distinguishable under all five investigated conditions, including the condition with the largest background fluctuation. An SNR of 22.98 dB represents the lowest value obtained in the present experiments. A value of 20 dB is used here only as a practical reference for discussing signal discernibility. It should not be regarded as a universal detection threshold for FBG-based impact monitoring. Since conditions with SNR below 20 dB were not systematically investigated, the identification limit under stronger interference remains to be determined. The present study provides an experimental basis for evaluating how mechanical-noise intensity and propagation path influence impact identification. Recent reviews have highlighted the broader role of optical-fiber sensing in structural feature identification, damage assessment, and structural state evaluation [32]. In this context, the present study provides an experimental basis for evaluating how mechanical-noise intensity and propagation path influence impact identification. Further work should introduce continuous vibration, random excitation, and multiple simultaneous disturbance sources. Benchmarking against a commercial FBG or other fiber-optic accelerometer would also provide a more appropriate basis for evaluating the dynamic performance of the proposed sensor.

5. Reference Measurement and Sensitivity Calibration Using a Commercial Accelerometer

5.1. Reference Measurement Using a Commercial Accelerometer

A commercial Hengxin Hongce 941B accelerometer was used as the reference instrument during the sensitivity calibration of the proposed FBG accelerometer. The two accelerometers were installed at structurally symmetric positions and subjected to the same periodic impact excitation. The acceleration measured by the 941B was used as the reference quantity, while the corresponding wavelength variation measured by the FBG accelerometer was used to determine the acceleration sensitivity.

The two accelerometers operate according to different sensing principles and signal-output schemes. The FBG accelerometer provides wavelength-based output in pm/g, whereas the 941B provides electrical output in V/g. These sensitivity values cannot be directly compared as equivalent sensor-performance metrics. The reference measurements presented in this section are therefore used to document the calibration-related experimental response rather than to establish a direct performance ranking between the two sensors.

5.2. Reference Responses Under the Experimental Conditions

The representative 941B measurements corresponding to the five experimental conditions are shown in Figures 11–15. These measurements were obtained under the same excitation conditions used for the FBG experiments and provide an external acceleration reference associated with the sensitivity-calibration procedure. The response characteristics observed from the 941B are presented for experimental context and to provide an external reference for evaluating its ability to detect impact events under the tested mechanical-noise conditions. No direct comparison of waveform shape or dynamic performance is made between the two accelerometers.

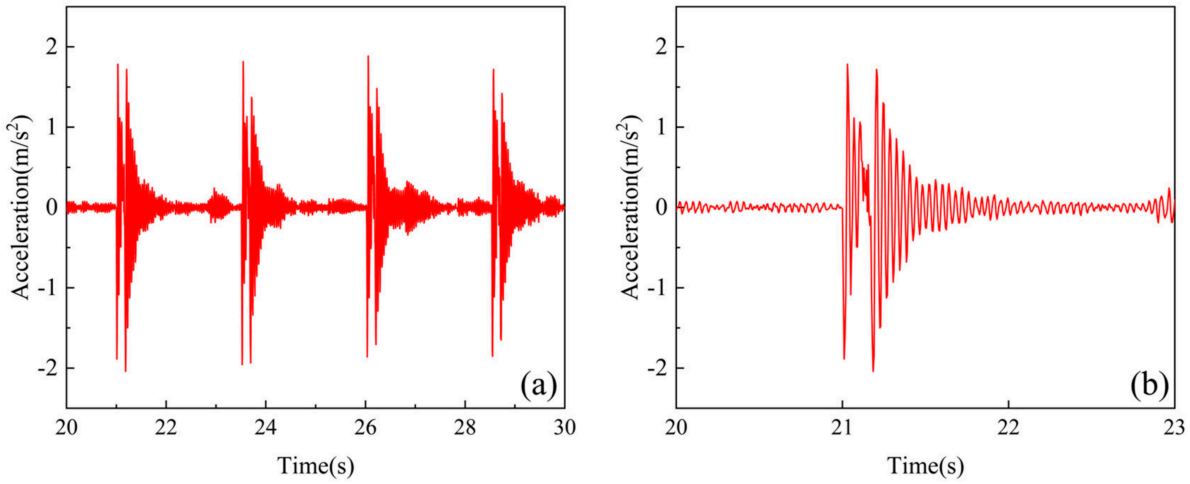


Figure 11. Representative (**a**) global and (**b**) local acceleration response measured by the commercial 941B accelerometer under the no-additional-mechanical-noise condition.

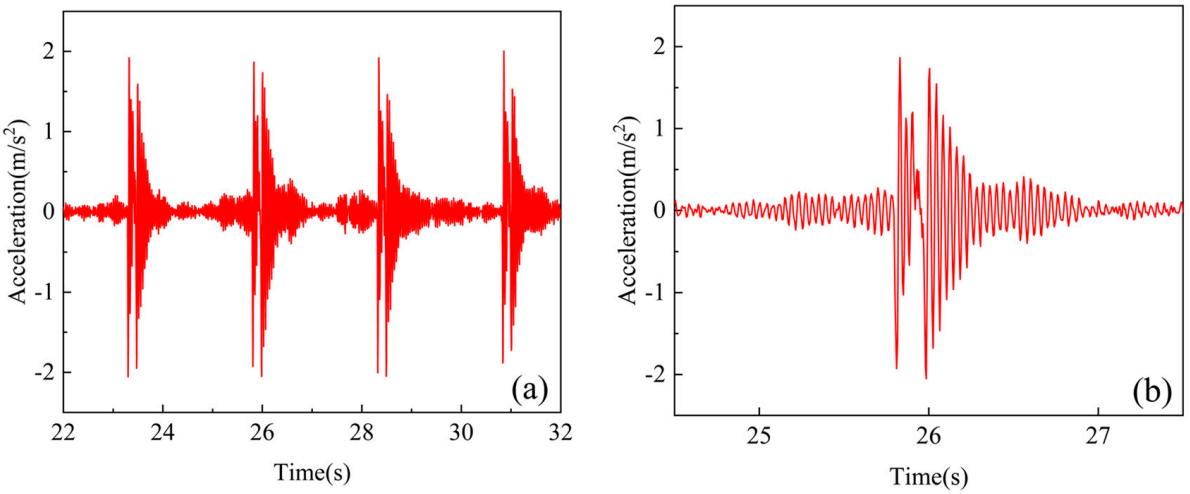


Figure 12. Representative (**a**) global and (**b**) local acceleration response measured by the commercial 941B accelerometer under Case 2 (low-intensity mechanical excitation of the pipe).

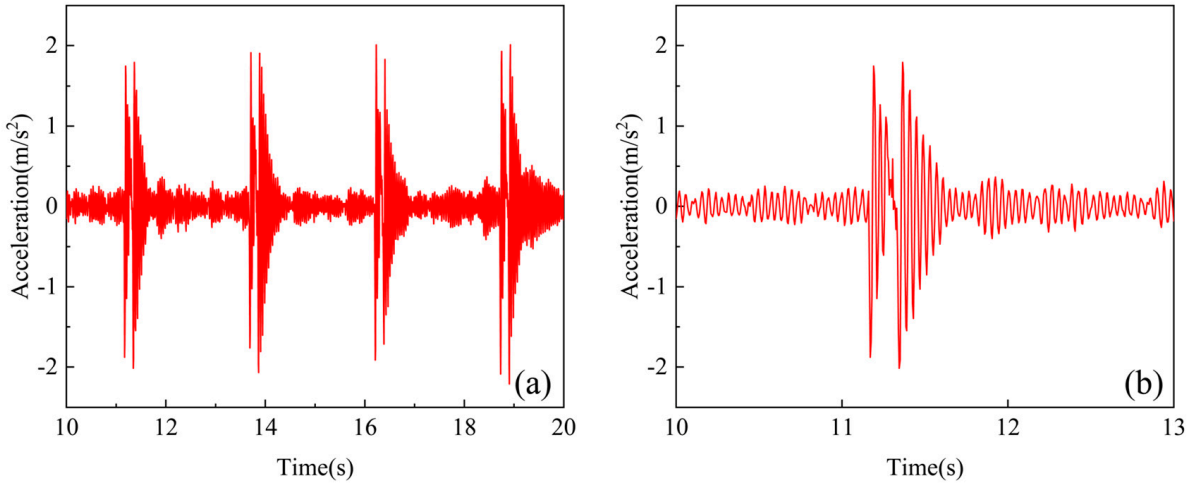


Figure 13. Representative (**a**) global and (**b**) local acceleration response measured by the commercial 941B accelerometer under Case 3 (low-intensity mechanical excitation of the test bench).

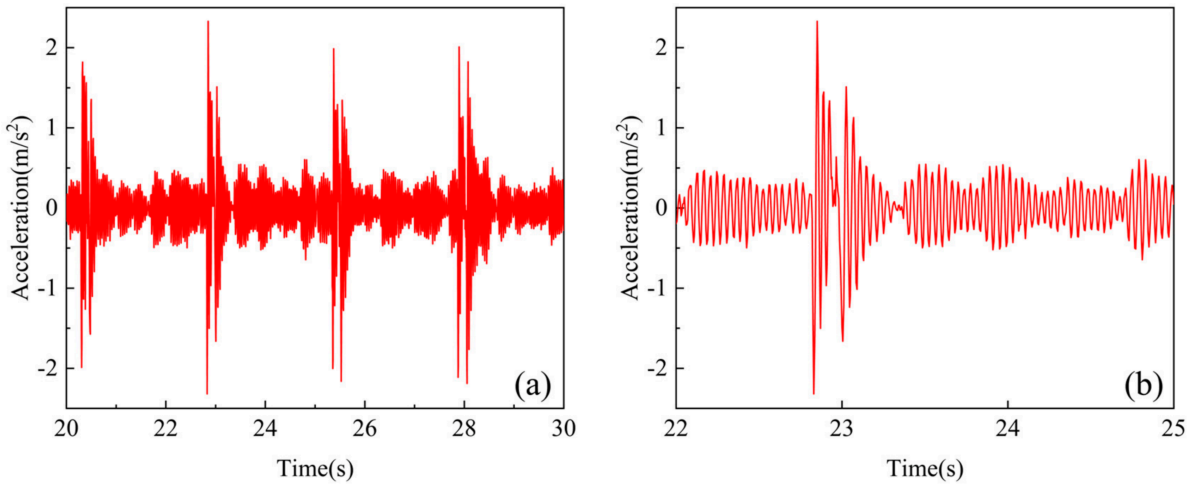


Figure 14. Representative (**a**) global and (**b**) local acceleration response measured by the commercial 941B accelerometer under Case 4 (high-intensity mechanical excitation of the pipe).

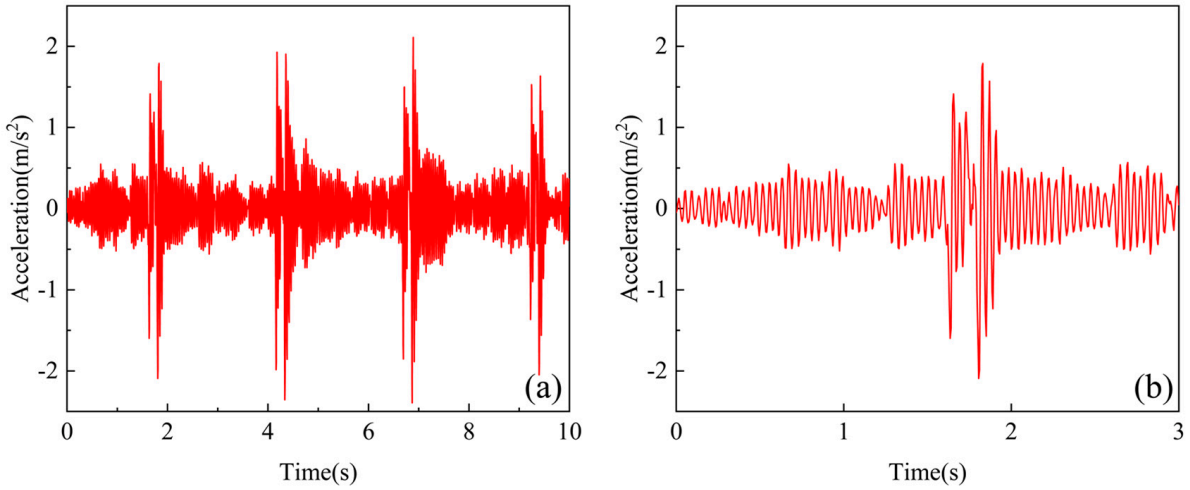


Figure 15. Representative (**a**) global and (**b**) local acceleration response measured by the commercial 941B accelerometer under Case 5 (high-intensity mechanical excitation of the test bench).

5.3. Scope and Limitations of the Reference Measurement

The reference measurements obtained from the 941B provide the acceleration values required for the sensitivity calibration of the proposed FBG accelerometer. They also document the response of the reference instrument under the corresponding experimental conditions.

The present study does not use the 941B measurements to claim that the proposed FBG accelerometer is superior or equivalent to the commercial accelerometer. The two devices have different sensing architectures and output forms, and the available measurements do not provide a basis for a complete cross-platform performance evaluation.

A more appropriate benchmark would use a commercially available FBG or other fiber-optic accelerometer with a comparable sensing mechanism and measurement configuration. Such a comparison will be considered in future work to further evaluate the dynamic characteristics and practical applicability of the proposed sensor.

6. Conclusions

This study experimentally investigated the impact response of a proposed FBG accelerometer under controlled mechanical-noise conditions. By varying the excitation inten-

sity and vibration propagation path, the effects of mechanical disturbance on background stability and target-impact response were characterized using wavelength-variation statistics, impact-response amplitude, and SNR. The results show that mechanical noise primarily increases background fluctuation, whereas the target impact response remains comparatively stable; under the most severe tested conditions, the SNR remained at 22.98 dB. These findings provide an experimental basis for evaluating the suitability of the investigated FBG accelerometer for impact monitoring in mechanically disturbed environments.

Future work should extend the experimental conditions to include continuous vibration, random disturbances, and multi-source coupled noise representative of real engineering environments. Further validation could also combine finite-element simulation, structural-dynamics analysis, and intelligent signal-processing methods with multi-point FBG sensor networks to assess the applicability of the sensor in large-scale structural health-monitoring systems.

Author Contributions: Conceptualization, Y.-H.L., H.-P.W. and P.X.; methodology, Y.-H.L. and Z.-J.J.; software, Y.-H.L. and C.-Y.G.; validation, Y.-H.L., Z.-J.J. and J.R.; formal analysis, Y.-H.L.; investigation, Y.-H.L. and J.R.; resources, Z.-J.J., X.-W.F. and J.-H.W.; data curation, Y.-H.L.; writing—original draft preparation, Y.-H.L.; writing—review and editing, Z.-J.J., H.-P.W. and P.X.; visualization, Y.-H.L. and C.-Y.G.; supervision, J.-H.W., H.-P.W. and P.X.; project administration, H.-P.W.; funding acquisition, J.-H.W., H.-P.W. and P.X. All authors have read and agreed to the published version of the manuscript.

Funding: This research was funded by the Innovation Foundation of Provincial Education Department of Gansu, grant number (2024B-005); the Fundamental Research Funds for the Central Universities, grant number (lzujbky-2024-05); the Industrial Support Plan Project of Provincial Education Department of Gansu, grant numbers (2025CYZC-003 and CYZC-2024-10); and the Scientific Department of Gansu, grant numbers (24CXGA083, 24CXGA024, JK2024-28, JK2024-32, 18YF1GA096 and 23CXJA0007).

Institutional Review Board Statement: Not applicable.

Informed Consent Statement: Not applicable.

Data Availability Statement: The data reported in the paper can be accessed from the corresponding authors.

Acknowledgments: Special thanks are due to Jinping Ou and Zhi Zhou of Dalian University of Technology, and Youhe Zhou and Xingzhe Wang of Lanzhou University. The findings and opinions expressed in this article are only those of the authors and do not necessarily reflect the views of the sponsors.

Conflicts of Interest: Z.J.J and J.R. are affiliated with Gansu Institute of Urban and Rural Planning and Design Institute Co., Ltd., X.W.F. is affiliated with Gansu Provincial Transportation Science Research Institute Group Co., Ltd., J.H.W. is affiliated with Gansu ZhiTong Technology Enginnering Detection Consulting Co., Ltd. The authors declare no conflicts of interest.The authors declare no conflicts of interest.

References

1. Wang, H.P.; Chen, C.; Ni, Y.Q.; Jayawickrema, M.; Epaarachchi, J. Computer-aided feature recognition of CFRP plates based on real-time strain fields reflected from FBG measured signals. *Compos. Part B Eng.* **2023**, *263*, 110866. [CrossRef]
2. Wang, D.; Wu, Y.; Song, Y.; Wang, Y.; Zhu, L. A double-mass block acceleration sensor based on FBG. *Opt. Fiber Technol.* **2021**, *66*, 102681. [CrossRef]
3. Liu, Q.; Qiao, X.; Jia, Z.; Fu, H.; Gao, H.; Yu, D. Large frequency range and high sensitivity fiber Bragg grating accelerometer based on double diaphragms. *IEEE Sens. J.* **2014**, *14*, 1499–1504. [CrossRef]
4. Xiao, X.; He, J.; Xu, X.; Chen, R.; Du, B.; Chen, Y.; Liu, S.; Fu, C.; Wang, Y. High-temperature-resistant fiber laser vector accelerometer based on a self-compensated multicore fiber Bragg grating. *Sensors* **2022**, *22*, 6459. [CrossRef] [PubMed]

5. Zhao, M.; Xie, Z.; Qi, Y.; Ou, Y.; Wang, S.; Zhu, Y.; Wei, X. A fiber optic Fabry-Pérot accelerometer for low-frequency and weak vibration detection. *Measurement* **2026**, *272*, 121013. [CrossRef]
6. Chen, R.; He, J.; Xu, X.; Xu, B.; Du, B.; Xiao, X.; Wang, Y.; Liao, C.; Weng, X.; Liu, L.; et al. Orientation-dependent accelerometer based on a highly localized fiber Bragg grating. *Opt. Laser Technol.* **2023**, *164*, 109464. [CrossRef]
7. Hasani, H.; Freddi, F.; Piazza, R.; Ceruffi, F. A wireless data acquisition system based on MEMS accelerometers for operational modal analysis of bridges. *Sensors* **2024**, *24*, 2121. [CrossRef] [PubMed]
8. Zhang, W.; Liu, X.; He, W.; Dong, M.; Zhu, L. Vibration monitoring for aircraft wing model using fiber Bragg grating array packaged by vacuum-assisted resin transfer molding. *Opt. Eng.* **2017**, *56*, 094102. [CrossRef]
9. Yassin, M.H.; Farhat, M.H.; Soleimanpour, R.; Nahas, M. Fiber Bragg grating (FBG)-based sensors: A review of technology and recent applications in structural health monitoring (SHM) of civil engineering structures. *Discov. Civ. Eng.* **2024**, *1*, 151. [CrossRef]
10. Zhou, C.; Jia, Z.; Song, S.; Luo, S.; Zhang, X.; Zhang, X.; Pei, X.; Xu, Z. Application of FBG sensor in health monitoring of engineering building structure: A review. *Sens. Rev.* **2025**, *45*, 129–145. [CrossRef]
11. Soman, R.; Moaf, F.O.; Fiborek, P.; Kudela, P.; Kurpińska, M. Investigating the suitability of the matched fiber Bragg grating approach for guided wave based structural health monitoring. *Measurement* **2025**, *242*, 115935. [CrossRef]
12. Guo, Y.; Chen, M.; Xiong, L.; Zhou, X.; Li, C. Fiber Bragg grating based acceleration sensors: A review. *Sens. Rev.* **2021**, *41*, 101–122. [CrossRef]
13. Hong, L.; Sun, R.; Qiu, Z.; Han, Z.; Li, Y. A multi-cantilever beam low-frequency FBG acceleration sensor. *Sci. Rep.* **2021**, *11*, 18502. [CrossRef] [PubMed]
14. Reghuprasad, A.E.; Colombero, C.; Godio, A. Serially connected cantilever beam-based FBG accelerometers: Design, optimization and testing. *Sensors* **2023**, *23*, 3188. [CrossRef] [PubMed]
15. Wang, X.; Zhang, R.; Fan, X.; Teng, Y.; Tang, Y. Miniaturized fiber Bragg grating accelerator sensors for low-frequency vibration monitoring. *Appl. Opt.* **2023**, *62*, 7254–7262. [CrossRef] [PubMed]
16. Zhang, Y.; Gao, H.; Zhang, L.; Liu, X. Design, simulation, and additive manufacturing performance of three lightweight FBG acceleration sensors. *Mech. Based Des. Struct. Mach.* **2024**, *52*, 9562–9586. [CrossRef]
17. Li, J.; Shen, B.; Zhang, H.; Song, Y. Fiber Bragg Grating Accelerometer and Its Application to Measure Wheel-Rail Excitation. *Struct. Control Health Monit.* **2024**, *2024*, 8442782. [CrossRef]
18. Chang, W.; Gong, H.; Fan, Q.; Xu, B.; Zhao, C. Fiber Bragg grating accelerometer based on asymmetric shaped flexible hinge structure. *Opt. Commun.* **2024**, *569*, 130855. [CrossRef]
19. Teng, Y.; Ge, L.; Fan, X.; Ge, C.; Ma, J. Dual straight-wing FBG accelerometer for low-frequency vibration measurement. *Opt. Commun.* **2024**, *563*, 130590. [CrossRef]
20. Li, H.; Zhang, X.; Gao, H.; Zhou, R.; Qiao, X. High sensitivity optical fiber accelerometer based on symmetric hinge structure with dual mass blocks. *Meas. Sci. Technol.* **2024**, *35*, 116005. [CrossRef]
21. Li, J.; Yu, Y.; Qing, X. Embedded FBG sensor based impact identification of CFRP using ensemble learning. *Sensors* **2021**, *21*, 1452. [CrossRef] [PubMed]
22. Huan, S.; Lu, L.; Shen, T.; Du, J. Low velocity impact monitoring of composite tubes based on FBG sensors. *Sensors* **2024**, *24*, 1279. [CrossRef] [PubMed]
23. Ding, G.; Chang, L.; Zhou, N.; Gao, X.; Li, M. Localization of low velocity impact on CFRP laminate using normalized error outlier-based algorithm cooperating with Db3-wavelet threshold noise reduction and FBG sensors. *Opt. Fiber Technol.* **2023**, *80*, 103455. [CrossRef]
24. Huang, J.; Yang, X.; Jiang, Q.; Zhang, L. Robust identification of impact force acting on composite structures via a single FBG sensor using variational mode decomposition. *Sci. Rep.* **2026**, *16*, 28624. [CrossRef] [PubMed]
25. Liu, Q.; Yu, Y.; Han, B.S.; Zhou, W. An improved spectral subtraction method for eliminating additive noise in condition monitoring system using fiber Bragg grating sensors. *Sensors* **2024**, *24*, 443. [CrossRef] [PubMed]
26. Dragomiretskiy, K.; Zosso, D. Variational mode decomposition. *IEEE Trans. Signal Process.* **2014**, *62*, 531–544. [CrossRef]
27. Zhang, W.; Zhang, M.; Zhao, Y.; Jin, B.; Dai, W. Denoising of the fiber Bragg grating deformation spectrum signal using variational mode decomposition combined with wavelet thresholding. *Appl. Sci.* **2019**, *9*, 180. [CrossRef]
28. Fallais, D.J.M.; Henkel, M.; Noppe, N.; Weijtjens, W.; Devriendt, C. Multilevel RTN Removal Tools for Dynamic FBG Strain Measurements Corrupted by Peak-Splitting Artefacts. *Sensors* **2022**, *22*, 92. [CrossRef] [PubMed]
29. Zhang, C.; Lai, S.X.; Wang, H.P. Structural modal parameter recognition and related damage identification methods under environmental excitations: A review. *Struct. Durab. Health Monit.* **2025**, *19*, 25–54. [CrossRef]
30. Shen, F.K.; Wang, S.K.; Zhang, J.Y.; Xia, Z.G.; Peng, B.R.; Sasy Chan, Y.W.; Xiang, P.; Wang, H.P. FBG Monitoring Information-Motivated Anti-Fatigue Performance Analysis of CFRP Composites Based on Non-Destructive Tests. *Polymers* **2025**, *17*, 1817. [CrossRef]

31. Tang, Y.Y.; Liu, Y.H.; Wei, D.Y.; Feng, X.W.; Campos e Matos, J.; Hui, D.; Wang, H.P. Analysis on impact resistance of smart CFRP laminates with embedded/surface-bonded FBG sensors. *Struct. Durab. Health Monit.* **2026**, *20*, 1. [CrossRef]
32. Wang, H.P.; Guo, C.Y.; Wei, D.Y.; Wang, X.Z.; Xiang, P.; Dai, J.G.; Ni, Y.Q.; Ou, J.P. Optical fiber sensing information driven structural feature parameter reflection, damage identification and state assessment: A review. *Chin. J. Appl. Mech.* **2026**, *43*, 748–766.

Disclaimer/Publisher's Note: The statements, opinions and data contained in all publications are solely those of the individual author(s) and contributor(s) and not of MDPI and/or the editor(s). MDPI and/or the editor(s) disclaim responsibility for any injury to people or property resulting from any ideas, methods, instructions or products referred to in the content.